Wenqi Ren
Department of Precision Machinery
and Precision Instrumentation,
University of Science and Technology of China,
Hefei 230027, China
e-mail: rwq1112@mail.ustc.edu.cn

Yingjie Qu
Department of Precision Machinery
and Precision Instrumentation,
University of Science and Technology of China,
Hefei 230027, China
e-mail: 1554046929@qq.com

Jiaojiao Pei
Department of Obstetrics and Gynecology,
Second Affiliated Hospital of Chongqing
Medical University,
Chongqing 400010, China
e-mail: 852975628@qq.com

Linlin Xiao
Department of Obstetrics and Gynecology,
Second Affiliated Hospital of Chongqing
Medical University,
Chongqing 400010, China
e-mail: xiaolinlinrachel@sina.com

Shiwu Zhang[1]
Department of Precision Machinery and
Precision Instrumentation,
University of Science and Technology of China,
Hefei 230027, China
e-mail: swzhang@ustc.edu.cn

Shufang Chang[1]
Department of Obstetrics and Gynecology,
Second Affiliated Hospital of Chongqing
Medical University,
Chongqing 400010, China
e-mail: shfch2005@163.com

Ronald X. Xu[1]
Department of Precision Machinery
and Precision Instrumentation,
University of Science and Technology of China,
Hefei 230027, China;
Department of Biomedical Engineering,
The Ohio State University,
Columbus, OH 43210
e-mail: xu.202@osu.edu

Development of a Multimodal Colposcopy for Characterization of Cervical Intraepithelial Neoplasia

To develop and evaluate the clinical application of a multimodal colposcopy combining multispectral reflectance, autofluorescence, and red, green, blue (RGB) imaging for noninvasive characterization of cervical intraepithelial neoplasia (CIN). We developed a multimodal colposcopy system that combined multispectral reflectance, autofluorescence, and RGB imaging for noninvasive characterization of CIN. We studied the optical properties of cervical tissue first; then the imaging system was designed and tested in a clinical trial where comprehensive datasets were acquired and analyzed to differentiate between squamous normal and high grade types of cervical tissue. The custom-designed multimodal colposcopy is capable of acquiring multispectral reflectance images, autofluorescence images, and RGB images of cervical tissue consecutively. The classification algorithm was employed on both normal and abnormal cases for image segmentation. The performance characteristics of this system were comparable to the gold standard histopathologic measurements with statistical significance. Our pilot study demonstrated the clinical potential of this multimodal colposcopic system for noninvasive characterization of CIN. The proposed system was simple, noninvasive, cost-effective, and portable, making it a suitable device for deployment in developing countries or rural regions of limited resources. [DOI: 10.1115/1.4036335]

Keywords: medical device, multispectral, autofluorescence, colposcopy, cervical intraepithelial neoplasia

1 Introduction

Cervical cancer has been the second most common type of cancer in women worldwide [1]. It is estimated that nearly 380,000 new cases are diagnosed each year, with more than 80% occurrence in the developing countries [2]. Early detection and treatment of precancerous lesions will prevent most cases of cervical cancer. Clinical approaches for screening CIN begin with an examination of Papanicolaou (Pap) smear. For patients with positive Pap smear results, a second visit must be scheduled 1–2 weeks later for colposcopy and directed biopsy in order to confirm a diagnosis of precancer. Biopsy results are typically unavailable until after 1–2 weeks. If high-grade precancer is identified by biopsy, treatment will be scheduled at a third visit [1]. The above paradigm has reduced the incidence of cervical cancer in many developed countries. However, many developing countries still lack the necessary infrastructure and resources for rapid, extensive, and low cost screening of the disease.

In the past few decades, technical advances in optical imaging have opened a new avenue for rapid, wide-field, and noninvasive assessment of cervical precancer, which have the potential to address the needs for CIN early screening in a rapid, cost-effective,

[1]Corresponding authors.

Manuscript received July 15, 2016; final manuscript received February 12, 2017; published online June 27, 2017. Assoc. Editor: Chris Rylander.

and noninvasive fashion [3–5]. Based on the changes in optical properties of neoplastic tissue, a number of imaging technologies have been investigated to enhance the contrast between normal and abnormal tissues. Among them, multispectral reflectance imaging acquires a series of images with global spectral information at multiple wavelengths and provides insight into multiple tissue characteristics such as tissue scattering and absorbing chromophore concentrations, particularly hemoglobin concentration and oxygenation levels [6]. Features of multispectral imaging have been further investigated in order to enhance the imaging contrast for tissue differentiation. For instance, reflectance imaging with green light illumination gives a better contrast because of hemoglobin absorption [7]. Illuminating tissue with polarized light will reduce specular reflection and improve visualization of subepithelial vessels [8]. Furthermore, based on diffuse reflectance spectroscopy or hyperspectral data cube, it is possible to extract a small number of specific wavelengths by dimensionality reduction to distinguish abnormal area at a lower computational cost. In the past few years, optical models based on Monte Carlo (MC) simulation and experimental measurements have been studied to reveal the disparities between normal and abnormal tissue reflectance characteristics [9]. Particularly, Zheng et al. proposed a wide gap second derivate method that used only three wavelengths between 600 and 800 nm for successful classification of the cervix tissue into three categories of normal, inflammation, and high-grade lesion [10].

Similar to spectral imaging, cervical autofluorescence can also be imaged in a wide-field mode for in vivo differentiation between normal and abnormal tissue types. Fluorophores contributing to tissue autofluorescence include nicotinamide adenine dinucleotide (NADH), flavin adenine dinucleotide, keratin, tryptophan, elastin, and collagen and their concentrations change with various diseases [11]. Generally speaking, normal cervical tissue yields greater fluorescence in stroma than that of cancerous tissue in the excitation wavelength range for ultraviolet (UV) (~330 to 370 nm) and green lights (~510 to 550 nm), inducing a negative contrast for the detection of precancerous lesions [12,13]. Zheng et al. used excitation–emission matrices to optimize the excitation light wavelengths for differentiation between normal and abnormal bladder tissues [14]. Schomacker et al. distinguished normal squamous tissue from CIN 2 and CIN 3 tissues based on their fluorescence spectra [15]. Thus, it is necessary to optimize the excitation and the emission bands for autofluorescence detection of cervical malignancy.

Combining different imaging modalities, multimodal imaging can provide a comprehensive assessment of multiple tissue parameters [16,17]. In the field of identifying cervical intraepithelial neoplasia, Chang et al. compared the performance characteristics of reflectance spectroscopy, fluorescence spectroscopy, and combinatory methods. They found that fluorescence spectra alone yielded more accurate diagnosis than those based on reflectance spectra alone, and that combination of fluorescence and reflectance information led to modest improvement in diagnostic accuracy [18]. However, this study was based on single point detection of tissue spectra and did not involve global imaging information of the tissue. Gustafsson et al. acquired the hyperspectral reflectance and fluorescence data cube of the entire cervical tissue separately, and demonstrated the spectral difference between different lesion types [19]. However, such a multimodal imaging system was expensive and the image coregistration was time consuming, inappropriate for deployment in developing countries and rural regions of limited resources.

We propose a portable multimodal imaging device that combines multispectral reflectance imaging, autofluorescence imaging, and RGB color imaging for real-time and noninvasive assessment of cervical tissue anomalies at low cost. In this multimodal imaging device, RGB imaging functions as a conventional colposcopy; multispectral reflectance imaging detects the functional characteristics of cervical tissue; and fluorescence imaging reveals the molecular signature of the lesion. In order to reduce the cost and the complexity of the system, we use only a single camera for all the imaging tasks without the need for coregistration. In this paper, we first established a mathematical model for light transportation in cervical tissue and optimized the working wavelengths for reflectance and autofluorescence spectral characteristics. Then, illumination characteristics of this system were validated. In clinical test, we determined the clinical protocol, the image processing algorithm, and the statistical analysis strategy for effective differentiation between squamous normal (SN) and high grade (HG) types of cervical tissue. After RGB, autofluorescence, and multispectral images were acquired by our multimodal colposcopic device, a second derivative method was applied to the multispectral data cube for feature extraction and a minimum distance method was used for image classification with training dataset according to the gold standard biopsy results. Statistically, the performance of the multimodal classification algorithm was evaluated by calculating the resultant sensitivity and specificity with respect to the gold standard. The effectiveness of autofluorescence imaging for the diagnosis of CIN was also compared. Our pilot study demonstrated the clinical potential of using this multimodal colposcopic system for in vivo characterization of CIN.

2 Materials and Methods

2.1 Model-Based Analysis and Working Wavelength Selection. In order to determine the working wavelengths for multispectral reflectance imaging and to optimize the combination of excitation and emission bands for autofluorescence imaging, the optical properties of SN and HG lesion tissue were studied based on proper optical models. Cervical tissue is composed of an epithelial layer on the top and a stroma layer at the bottom. The development of cervical precancer leads to changes in the structural and optical properties of both layers [1]. The geometry of the SN and HG tissue in our optical model was established as shown in Fig. 1(*a*), with anisotropy $g = 0.95$ for the first layer and $g = 0.88$ for the second layer, refractive index $n = 1.4$ for both layers, 300 μm thickness for the normal epithelium and 500 μm thickness for the abnormal epithelium. The absorption coefficient (μ_a) and the scattering coefficient (μ_s) of SN and HG tissues between 500 nm and 600 nm were available in the literature and were reproduced in Figs. 1(*b*) and 1(*c*) with an assumption of 85% hemoglobin oxygen saturation [20]. All these parameters were used as inputs for MC simulation of cervical tissue reflectance spectrum and the simulation results were compared with those of an analytical model. Fluorescence characteristics of normal and abnormal tissue were further investigated in order to optimize the selection of excitation and emission wavelengths.

2.1.1 Monte Carlo Simulation and Analytical Model for Cervical Diffuse Reflectance. As a flexible approach to study photon propagation, a modified two-layered Monte Carlo code based on Ref. [21] was developed for tissue diffuse reflectance simulation between 500 nm and 600 nm in 2 nm increments. In comparison, an analytical expression based on diffuse theory was implemented to calculate the reflectance spectrum of cervical tissue model in a simple manner. The approximation expression is shown as below:

$$R = R_s + \frac{(1 - R_s)(1 - s)(1 - b_1 s)}{1 + b_2 s} \tag{1}$$

where $R_s = ((n-1)^2/(n+1)^2)$, $s = \sqrt{(\mu_a/\mu_a + \mu_s')}$, n is the refractive index, μ_a is the absorption coefficient, $\mu_s' = (1-g)\mu_s$ is the reduced scattering coefficient, b_1 and b_2 are two constants associated with anisotropy factor g. More details can be seen in Ref. [22]. All the necessary parameters shown in Fig. 1 were fed into the program and expression. For MC simulation, each simulation has been performed using 20K input photons.

To minimize the number of wavelengths used for reflectance imaging, a wide gap second derivative method was deployed to analyze the simulated reflectance above. This method was capable of removing both baseline offsets depending upon whether the

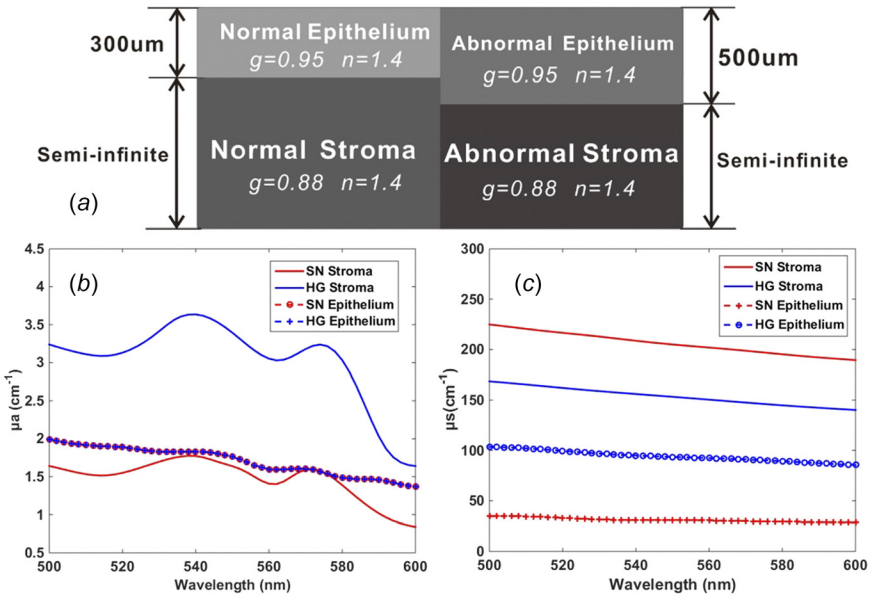

Fig. 1 (*a*) Geometry of the cervical tissue model. The cervical tissue is composed of two layers: epithelium and stroma. The thickness of abnormal epithelium layer is a little larger than that of normal epithelium and the stroma is thought as semi-infinite. (*b*) Absorption coefficients of SN and HG tissues. (*c*) Scattering coefficients of SN and HG tissues.

spectrometer device is calibrated, whether detection gain remains fixed, and linear slope due to the wavelength-dependent scattering [23]. Meanwhile, the measurement error resulted from nonuniform illumination can also be corrected. With a fixed wavelength gap interval $\Delta\lambda$, the second derivative value of wavelength λ, i.e., $R(\lambda)''$, was calculated by the reflectance intensity R of three wavelengths as follows:

$$R(\lambda)'' = \frac{R(\lambda+\Delta\lambda) + R(\lambda-\Delta\lambda) - 2R(\lambda)}{2\Delta\lambda} \tag{2}$$

Then, proper wavelengths set and gap interval $\Delta\lambda$ were derived based on the wide gap second derivative spectrum to extract the difference of reflectance between normal and abnormal cervical tissues. A screening filter as described in Ref. [10] was employed to acquire the best spectral configuration with superior capability of tissue classification.

Figure 2(*a*) compares the relative reflectance intensity of MC simulation and the analytical model from 500 nm to 600 nm. The latter results were normalized with respect to the MC results at the wavelength of 500 nm. According to the figure, the analytical results agree well with the numerical results, indicating the reliability of the established analytical model. The second derivative reflectance spectra are plotted in Fig. 2(*b*). Based on the screening filter described in Ref. [10], a wavelength combination of 545 nm, 560 nm, and 575 nm will differentiate between normal and abnormal cervical tissues significantly. To reach these three central wavelengths, five wavelengths ranging from 530 nm to 590 nm at an interval of 15 nm were selected for wide-gap second derivative reflectance imaging.

2.1.2 Autofluorescence Characteristics of the Cervical Tissue. A number of optical models and experimental trials have been investigated to optimize the excitation and emission wavelengths for cervical autofluorescence diagnosis. Theoretically, a two-layer analytical model and a Monte Carlo simulation model were compared in Ref. [24] to describe fluorescence spectra of normal and preneoplastic epithelial tissues. Besides, based on the clinical

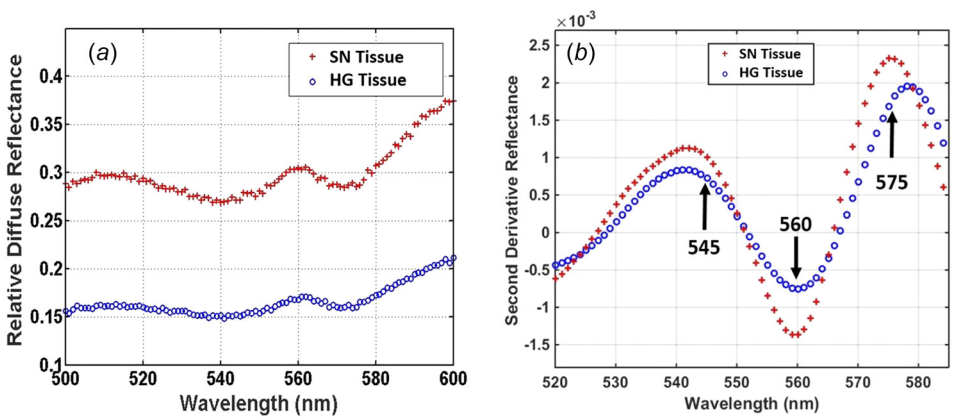

Fig. 2 (*a*) Monte Carlo simulation and analytical model results of cervical tissue reflectance spectrum. (*b*) Second derivative reflectance spectrum based on MC simulated results. Three significant disparate points at 545 nm, 560 nm, and 575 nm are indicated for discrimination between normal and abnormal tissues.

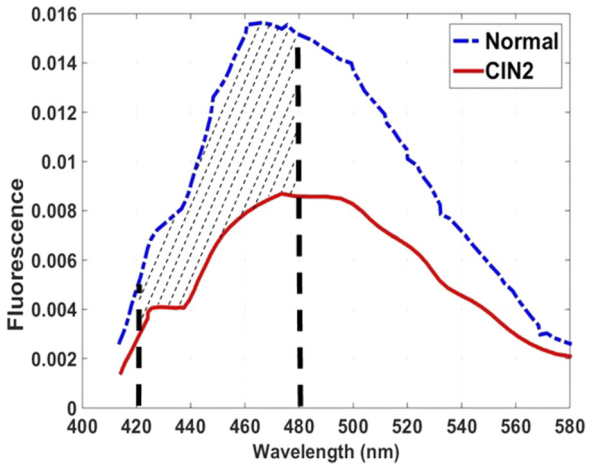

Fig. 3 Cervical autofluorescence spectra at 365 nm excitation. The figure is modified based on Ref. 25. The shaded area shows the fluorescence intensity disparity between normal and abnormal tissues.

measurements, cervical autofluorescence data can be represented as an excitation–emission matrix (EEM), where the emission spectra at the various excitation wavelengths are concatenated into a 2D matrix so that the calibrated fluorescence intensity can be expressed as a function of excitation and emission wavelengths. To determine the specific excitation wavelength and collection wavelength range for our colposcopy design, we referred to the work reported by Parker in 2002, where an excitation wavelength at 365 nm and an effective emission range from 445 to 475 nm were used for tissue anomaly differentiation [25].

Figure 3 compares the fluorescence spectra of normal and abnormal tissues at an excitation wavelength of 365 nm. The shaded area demonstrates the disparity of fluorescence intensities between different tissues. Quantitatively, the enveloping area of the fluorescence spectrum for normal tissue is 61.17% greater than that of abnormal tissue, corresponding to a greater fluorescence emission in the acquired autofluorescence images. Based on the above analysis and the consideration of commercial availability for the specific optical components, we finally determined the excitation wavelength of 365 nm and the fluorescence detection band from 420 nm to 480 nm for our multimodal colposcopic device.

2.2 Instrumentation Design. A multimodal colposcopy system as depicted in Fig. 4 has been developed for comprehensive assessment of cervical tissue lesions. The system is composed of three modules: (1) a colposcopy consists of a multispectral narrow band LED light source, a band pass fluorescence filter with rotatable holder, and a monochromatic CCD camera with a prime lens; (2) a multichannel light source controller used for power supply and channel selection; and (3) a laptop used for system control and data acquisition.

The multispectral light source contained eight groups of specific narrow band ultrabright LEDs (Xilan Photoelectricity Group, China) including 365 nm, 475 nm, 530 nm, 545 nm, 560 nm, 575 nm, 590 nm, and 635 nm wavelengths. Each group consisted of eight same LEDs equally distributed along a ring-shaped aluminum substrate as shown in Fig 2(*b*). Among them, the 365 nm LEDs were used for autofluorescence excitation; the 475 nm, 545 nm, and 635 nm LEDs were used for RGB image illumination; and the rest LEDs were used for multispectral illumination. A piece of ground glass was covered on the light source for uniform illumination. The band pass filter (420–480 nm band pass, Rayan Technology Co., Ltd., Changchun, China) with a rotatable mount was used for cervical tissue autofluorescence collection. When the excitation light (365 nm) was on, the filter would be rotated and the optical path would be blocked, otherwise the filter would be off due to the optical path. The monochromatic CCD camera (Microvision Digital Imaging Technology Co., Ltd., Xian, China) with a 50 mm focal prime lens was used for imaging with a maximum resolution of 1392×1040 pixels. The quantum efficiency of the CCD chip was greater than 50% at a wavelength range from 400 nm to 650 nm, which was suitable for multispectral and fluorescence images collection. The light source controller (OPT Tech Co., Ltd., Shenzhen, China) was connected to the laptop via RS232 serial port for intensity adjustment and channel selection, which was capable of providing 24 V power supplies for eight channels separately.

For the sake of exposure control and image transmission, the camera was connected to an image grabber through a 1394 A port. The operation of the whole system was controlled using a LABVIEW-based program (National Instruments, TX) running on the laptop. Figure 4(*c*) shows the photography of the multimodal colposcopy system.

To validate the system, especially the performance of multispectral light source, we measured the relative spectral power distribution of the LEDs at every wavelength using a USB4000 spectrometer (Ocean Optics, FL). Then, the illumination effect was simulated in TRACEPRO software (Lambda, MA) by geometry

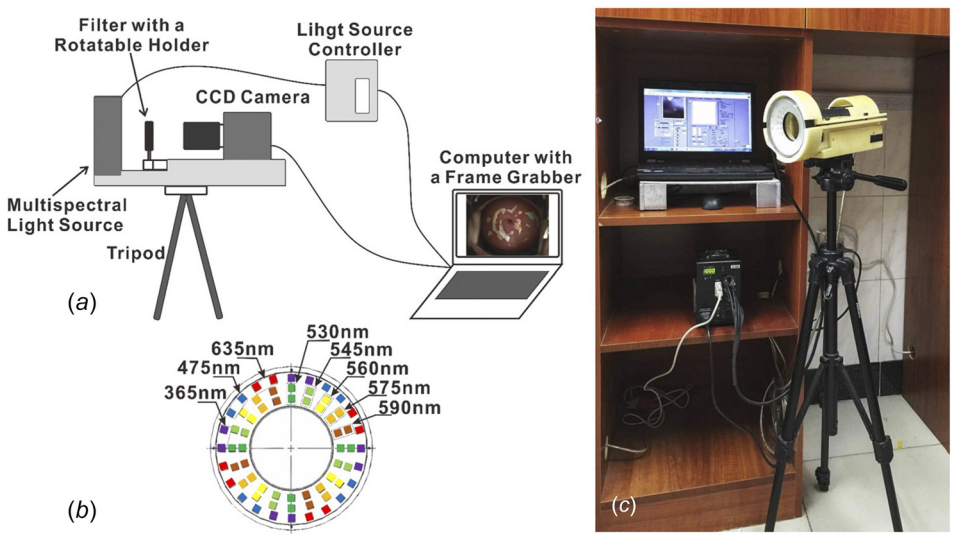

Fig. 4 System diagram of the multimodal colposcopy: (*a*) diagram of the multimodal colposcopy system, (*b*) front view of the multispectral LED light source, and (*c*) photography of the multimodal colposcopy system

modeling, properties defining, and raytrace. Furthermore, the simulative result was compared with experimental result to validate uniform illumination intensity in the field of view.

2.3 Clinical Protocol. The clinical protocol was reviewed and approved by the Institutional Review Board (IRB) of the Second Affiliated Hospital of Chongqing Medical University (IRB No: 2013KLS002). Eligible patients recruited in this study were nonpregnant women over the age of 18 who were referred to the colposcopy clinic due to an abnormal result of liquid-based cytology. Most of these abnormal cases were identified as CIN 2/3 and a few of them were identified as CIN 1 or cervicitis that required further operation of loop electrosurgical excision procedure (LEEP). All the patients participating in the study signed an informed consent form and underwent a LEEP after the session of multimodal image acquisition. Before formal acquisition, a 4 mm × 4 mm white Teflon board with black cross marker at the center was placed on the cleaned cervical surface to help focusing and spectrum correction. The spectral characteristics of Teflon board were calibrated in advance by a NIST traceable white diffuser (NIST, Gaithersburg, MD). After the refined focusing and pre-exposure procedure, the Teflon board was removed and the clinical data were collected following the consecutive steps as described below:

(1) Acquiring the background images with the environmental lights on and the colposcopy light off.
(2) Acquiring multispectral reflectance images, autofluorescence images, RGB images, and green channel enhanced images sequentially. Each imaging session was triplicated in order to reduce the measurement error.
(3) Applying acetic acid (5%) on the cervix for 50 s and capturing RGB images at 60 s, 120 s, 150 s, and 180 s, respectively. The one with most observable whitening phenomenon would be used for clinician's reference.
(4) Recording the RGB images as Lugol's iodine was applied.

After the above multimodal imaging collection session, the LEEP procedure removed a portion of the cervix starting from the 9 o'clock clockwise. Immediately after the procedure, the sample was stained and a stitch was placed at each clock position. The sample was fixed in formalin and sectioned radially into 12 specimens for histopathologic examination of lesion distribution in every section. In this way, our image segmentation results were correlated with the pathological results in every clock direction. The diagnostic categories included normal (normal epithelium, inflammation, and CIN 1) and HG (high grade, including CIN 2 and CIN 3) tissue types.

2.4 Image Processing

2.4.1 Image Preprocessing. Our device used only a single imaging module to avoid coregistration difficulties. During the process of clinical data collection, the patients were required to keep still to allow for acquisition of one complete set of multimodal images. Consequently, some acquired images have poor imaging quality due to unexpected motion artifacts, which should be excluded out of this study. For minor motion artifacts between multispectral, fluorescence, and RGB imaging modalities, we used the coregistration function of IMAGEJ software to correct the minor motion artifacts and guarantee the image quality.

For the multispectral reflectance images, the first step of image preprocessing was to remove noise interference by image averaging and background subtraction as Eq. (3), where $R_{\text{raw}}(\lambda)$ denotes the reflectance intensity of raw images collected by our system, $R_{\text{bg}}(\lambda)$ denotes the background images acquired with constant room lights. $\bar{R}(\lambda)$ was averaged from three continuous acquired images for denoising

$$\bar{R}(\lambda) = \sum_{n=1}^{3} \frac{R_{\text{raw}}(\lambda) - R_{\text{bg}}(\lambda)}{3} \tag{3}$$

Then, the multispectral reflectance images were corrected using a Teflon board to remove the influence of inconsistent reflectivity at different wavelengths. The corrected reflectance $R(\lambda)$ is expressed as Eq. (4), where R_{board} is the mean intensity of a region of interest (ROI) selected on the surface of the Teflon board

$$R(\lambda) = \frac{\bar{R}(\lambda)}{R_{\text{board}}} \tag{4}$$

For autofluorescence images, background subtraction and image averaging were also performed for denoising. Then, the histogram was equalized for better contrast.

For RGB images, one color image was generated by recoding three eight-bit monochrome images acquired at red, green, and blue illumination into a 24-bit true color image, which realized the visualization of color and morphological characteristics of cervical surface.

2.4.2 Classification Algorithms. In order to identify the abnormal areas on cervix, each pixel of a cervical image was classified to be either SN or HG according to a classification algorithm. Our approach for image segmentation consists of two major steps. First, a supervised classification algorithm was performed utilizing the second derivative multispectral reflectance images. Second, a simple correcting process was performed using the autofluorescence images.

In the first classification step, the classifier was trained using leave-one-patient-out cross-validation. The training sets including background (BG), SN, and HG were selected on a patient with local CIN 2/3 lesion and then applied to the held-out patient. Then three second derivative images were deduced from the raw reflectance images at five specific wavelengths according to Eq. (2). The absolute values of three derived intensities were summed and a minimum Euclidean distance (MD) segmentation algorithm was adopted for classification. The distance can be calculated as

$$D_{Ex} = \sqrt{\sum_{i=1}^{p} (R_{si} - R_{ti}^{x})^2} \tag{5}$$

$$C_x = \min(D_{Ex}) \tag{6}$$

where R_{Si} is the summed second derivative value of each pixel on the image and R_{ti}^{x} is the training data of three tissue types, here $x = (1, 2, 3)$ indicates the index of the three different tissue categories. D_{Ex} is the Euclidean distance and C_x indicates which category R_{si} is classified to by evaluating the minimum value D_{Ex}. The classifier designed with training set data was then used to classify entire images into corresponding categories. While in the second step, the autofluorescence images were binarization processed to create a mask for first-step results correction, where the threshold was determined by the disparity of tissue's fluorescent intensity between normal and abnormal tissues. As a comparison, we showed the segmentation results with and without autofluorescence correction in the results.

2.5 Statistical Analysis. To assess the diagnostic performance of the classification algorithms described above, a patient-based approach for calculating sensitivity and specificity was used according to Eqs. (7) and (8). In this approach, if a result image contains an area of abnormal greater than 20% pixel number of the whole picture, the patient was classified as a HG patient [26]. Additionally, to determine the most desirable sensitivity and specificity values, and to compare the diagnostic performance with and without autofluorescence assistant judgment, the receiver operating characteristic (ROC) curves were plotted

$$\text{Sensitivity} = \frac{\text{number of patients correctly identified as HG}}{\text{number of HG patients according to biospy}} \tag{7}$$

$$\text{Specificity} = \frac{\text{number of patients correctly identified as SN}}{\text{number of SN patients according to biospy}} \tag{8}$$

3 Results and Discussion

3.1 Instrument Validation. The most important characteristic of this custom-designed multimodal colposcopy is its multispectral illumination. Figure 5 shows the relative spectral power distribution of the multispectral LED light source at every wavelength. Among them, the shifts between realistic and ideal central wavelength are less than 5 nm, and the full width at half maximum (FWHM) are less than 35 nm. Therefore, the wavelength property of this multispectral light source is reliable.

One the other hand, the light source illumination uniformity was also verified by software simulation and experiment test, respectively. Figure 6(*a*) illustrates the geometry model and ray trace in TRACEPRO, and the corresponding illuminance distribution map on a circular observe plane is rendered in Fig. 6(*b*). Then, we plotted the intensity profile on its central line and compared it with experimental test result with the same conditions. The plots are shown in Fig. 6(*c*) and it is witnessed that the intensity profiles are even enough and agree well, indicating the illumination uniformity of our light source.

3.2 Patients Characteristics. A total of 48 patients were evaluated at Second Affiliated Hospital of Chongqing Medical University. All of them are Asian people and their age range from 26 to 49. However, 11 patients were excluded from the study because of the lack of biopsy results or the poor imaging quality due to irretrievable motion artifacts. The other 37 data sets consist of a series of multimodal images dataset that were deemed adequate for both reflectance and fluorescence images analysis by independent reviewers. Based on the inspection of the LEEP specimens, patients with acute/chronic inflammation, metaplasia, or CIN 1 were included in the normal category (five patients, 13.5%). Meanwhile, patients with any CIN 2 and CIN 3 diagnostic were included in the corresponding abnormal category (32 patients, 86.5%).

3.3 Imaging Results

3.3.1 Multimodal Images Dataset. A typical raw multimodal image dataset is shown in Fig. 7. The figure is arranged by the acquisition steps from top to bottom. The top row displays the cervical images without applying any agent, including monochromatic background image without light illumination, RGB image of cervix, green channel enhanced color image, multispectral reflectance images, and autofluorescence image. The lower right box indicates the preliminary process results of multispectral images, showing eight sites belonging to normal/abnormal types depending on the biopsy results in different colors. Corresponding reflectance curves are plotted on the right side. The second and third rows illustrate the postacetic acid and post-Lugol's iodine RGB images of cervix, respectively, which can be used for clinical auxiliary diagnosis as general digital colposcopy.

One advantage of acquiring images in multiple modalities using an integrated imaging system is the elimination of the time-consuming image coregistration process. Besides, since all the images were acquired by a single imaging module at preset operating parameters, the potential mismatch between different imaging modalities can be eliminated and the testing time for each patient can be further reduced.

3.3.2 Image Segmentation Results. Based on the multispectral reflectance data, the image classification algorithm as described in Sec. 2.4.2 was applied for image segmentation and distinction between normal and abnormal cervical tissue types. In addition, autofluorescence images were also analyzed for supplementary correction of the segmentation results. Furthermore, the image classification results of each patient were compared with their gold standard histopathology. In our study, the training sample was from a patient with local CIN2/3 lesion on 5 and 8 o'clock. For each classification category, three 20×20 pixel windows were on corresponding areas selected as training data set. After image classification, we correlated the pathological results with our image segmentation results in every clock direction. The accuracy of our image segmentation results can be evaluated intuitively.

Figure 8 shows the images and analyzed results of a patient with a CIN lesion at 7 o'clock and 8 o'clock according to the histopathologic result. The upper row images are RGB images of cervix without applying any agent, with green channel enhanced, with acetic acid, and with Lugol's iodine, respectively. The lesions can be visualized empirically in Figs. 8(*c*) and 6(*d*), where a whitening area postacetic acid and a lightly dyed area post-Lugol's iodine were revealed. Figure 8(*e*) shows the second derivative image of the multispectral dataset. Based on this data, the segmentation results of the classification algorithm when classifying SN, HG tissue, and BG can be seen in Fig. 8(*f*). The largest areas correspond to SN, the smallest areas correspond to HG and the other areas to BG. According to Fig. 8(*f*), one can see tolerable correlation between the classification results and the pathology results despite some false positive areas at 5, 6, 11, and 12 o'clock. Furthermore, Fig. 8(*g*) shows the autofluorescence image at 365 nm excitation. When we take the diagnostic effect of autofluorescence into account, the segmentation results are modified as shown in Fig. 8(*h*), which reveals a better segmentation image corresponding to the pathology results.

Similarly, Fig. 9 shows the images of a patient without CIN lesion but only chronic cervicitis according to the LEEP specimen

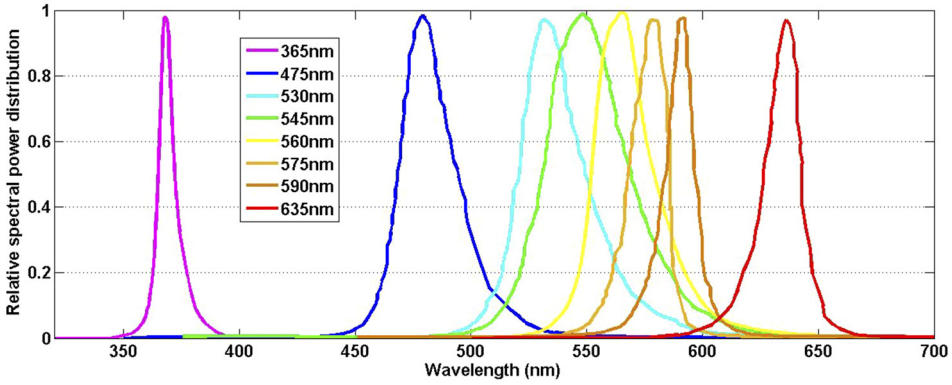

Fig. 5 The relative spectral power distribution of the multispectral LED light source. Among them, the 365 nm light is used for autofluorescence excitation; the 475 nm, 545 nm, and 635 nm light are used for RGB image illumination; and the rest are used for multispectral illumination.

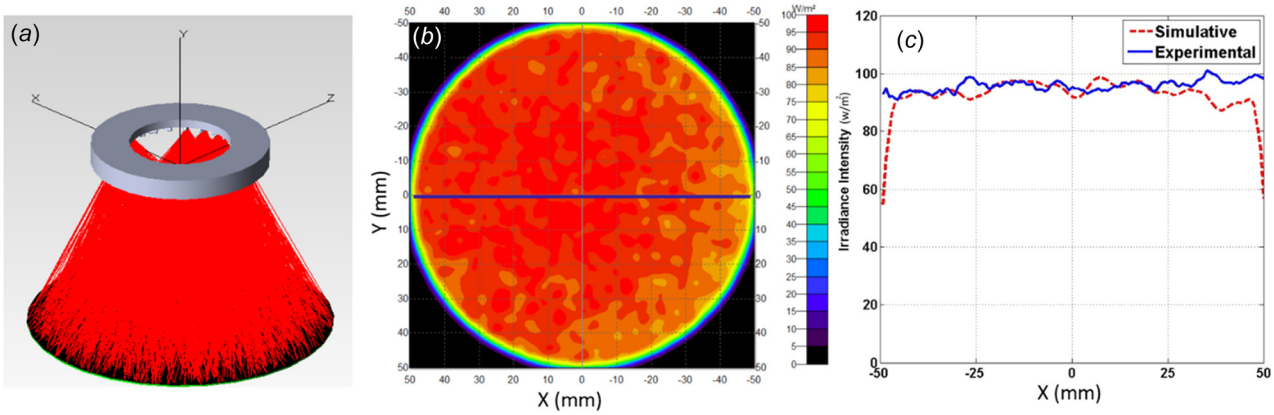

Fig. 6 Validation of light source illumination uniformity: (*a*) illumination simulation model in TRACEPRO software, (*b*) the simulative illuminance distribution map on an observe plane, and (*c*) comparison of the central line intensity profile between simulation and experimental measurement

inspection. Intuitively, the acquired RGB images in the upper row show no distinct suspicious regions with the use of green illumination filter and basic agent. According to the image segmentation result processed from multispectral reflectance data, Fig. 9(*g*) shows that the entire cervical tissues except several sites at 1 o'clock and 7 o'clock are diagnosed to be normal. To minimize the analysis error, the autofluorescence image was utilized to create a mask for optimal segmentation results. Figure 9(*h*) shows that the segmented images after autofluorescence correction correlate well with the pathology results.

According to the above analysis, information provided by RGB imaging, multispectral imaging, and autofluorescence imaging is complementary. RGB imaging is an empirical procedure that reveals some but not all information about tissue physiopathologic condition. Particularly, the unrealistic color pattern of the RGB images as shown in Figs. 8 and 9 is caused by the unbalanced illumination and detection at different wavelengths and can be further fixed by optimizing the LED and the detector designs in the future. Multispectral imaging reveals tissue functional properties, while autofluorescence imaging reveals tissue molecular characteristics. In Fig. 8(*f*), multimodal imaging yields a region of tissue anomaly greater than that of pathology, indicating that classification strategy is overtrained that may lead to lower specificity but higher sensitivity. By enhancing the autofluorescence image in Fig. 8(*g*), one is able to obtain appropriate classification of the lesion location coincident with pathology, as shown in Fig. 8(*h*). In addition to classification, we have also explored several other image processing approaches for effective interpretation of multimodal colposcopic images [18,26–29]. As a comparison, the classification algorithm implemented in this system shows its

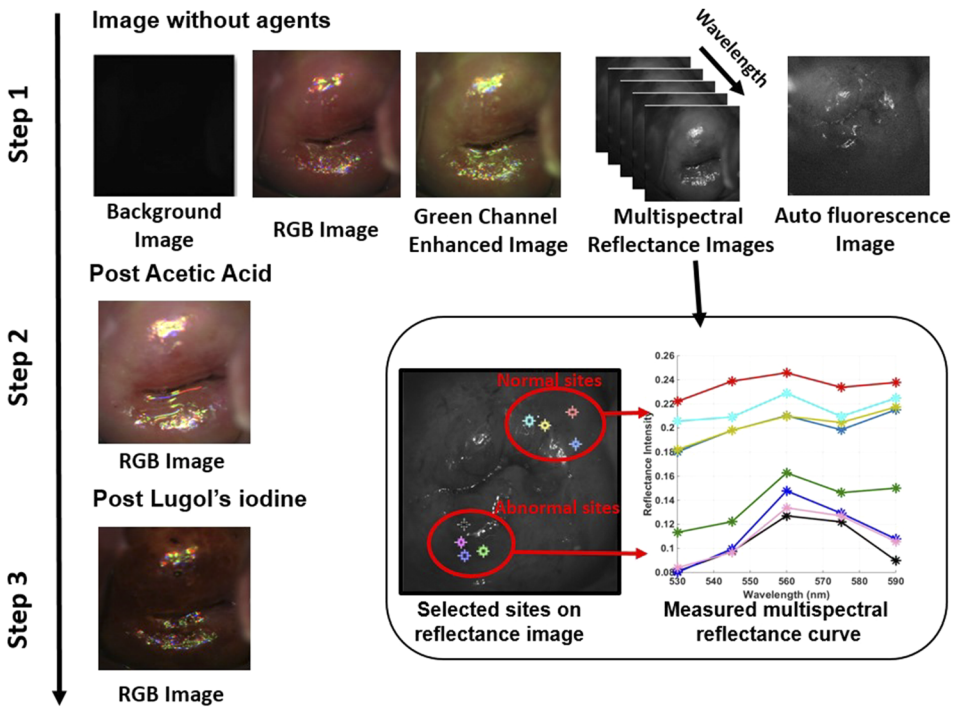

Fig. 7 A typical raw multimodal images dataset. The top row displays the cervical images without applying any contrast agent, the second and third rows illustrate postacetic acid and post-Lugol's iodine RGB images of cervix, respectively. The lower right box indicates the preliminary process results of multispectral data.

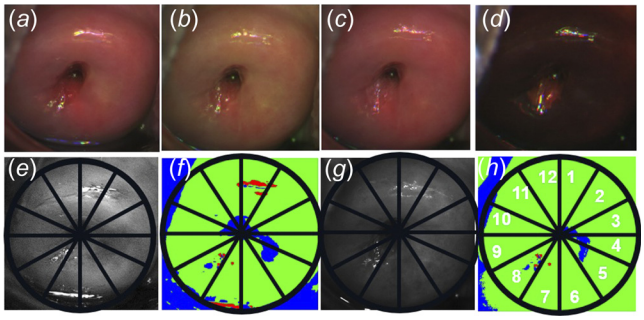

Fig. 8 Images of a CIN patient case: (*a*) RGB image, (*b*) green channel enhanced RGB image, (*c*) RGB image postacetic acid, (*d*) RGB image post-Lugol's iodine, (*e*) multispectral image after second derivative process, (*f*) segmentation image based on reflectance images, (*g*) enhanced auto fluorescent image, and (*h*) corrected segmentation result based on fluorescence. The pathology section codes on lower row are used to correlate the pathology diagnosis to the images. The segmentation images have three parts: background area, normal tissue (largest areas) and abnormal tissue (smallest areas), respectively.

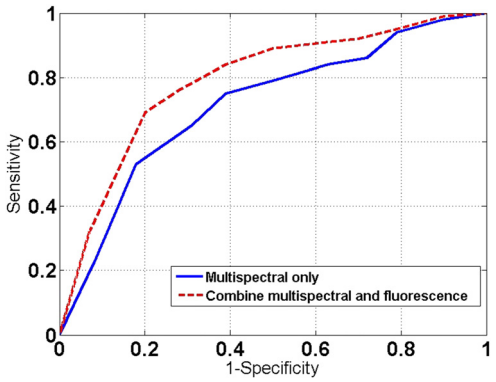

Fig. 10 ROC curves for classifier discrimination of HG versus SN sample for different assessment methods. The solid line plots the results calculated from multispectral images only. The dotted line plots the results calculated by combining multispectral and fluorescence images together.

diagnostic potential by combining cervical reflectance and auto fluorescence characteristics together. However, the quantitative discrimination algorithm especially based on the autofluorescence characteristic should be studied in future.

3.4 Statistical Analysis. The performance of the proposed classifier algorithm with and without fluorescence correction was evaluated and the resulting ROC curves were plotted. As shown in Fig. 10, the ROC curve achieved using only multispectral reflectance data yields decent performance by the segmentation algorithm. The area under curve (AUC) is calculated to be 0.714. The cutoff point, i.e., maximum of the sum of sensitivity and specificity, of this method corresponds to a sensitivity of 75% and a specificity of 60%. In contrast, the performance of comprehensive method combined with autofluorescence judgment is better, i.e., an AUC of 0.792, a sensitivity of 74%, and a specificity of 80%.

However, the sensitivity of our device is relatively low. This is possibly associated with the type of the transformation zone for the patients. It is known that the sensitivity of colposcopy is relatively high on patients with type I and type II transformation zones. For patients with type III transformation zone, the sensitivity of colposcopy may decline since the lesions are located in the cervical canals instead. Due to the limited number of patients involved in our study, the statistical analysis did not include the type difference of the cervical transformation zone, leading to possibly low sensitivity of our device. In the future work, we will increase the number of patients and consider different transformation zone types in order to achieve better statistical analysis.

The results obtained from this pilot study are statistically significant despite the fact that a small number of patients were recruited for the study. In our pilot study, we evaluated the performance of this device using a "number of patients" metric. Compared with pixel-based analysis methods, this is a simplified but still valid method for evaluating the accuracy of our device. In our future work, we would like to calculate the sensitivity and specificity based on image analysis for individual patients. In comparison with the conventional diagnostic method in a clinic setting, the classification algorithm based on second derivative multispectral images provides acceptable diagnostic effectiveness for the discrimination of SN and HG tissues in spite of a relative

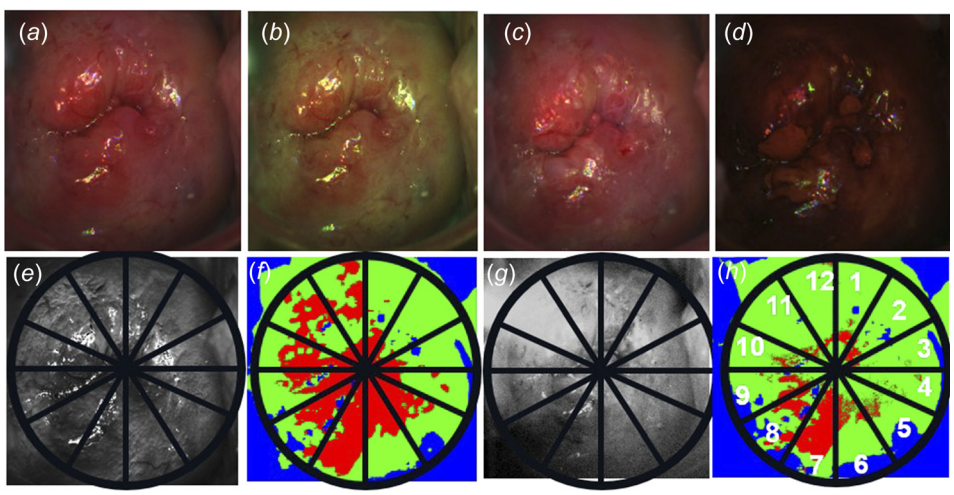

Fig. 9 Images of a normal patient case: (*a*) RGB image, (*b*) green channel enhanced RGB image, (*c*) RGB image postacetic acid, (*d*) RGB image post-Lugol's iodine, (*e*) multispectral image after second derivative process, (*f*) segmentation image based on reflectance images, (*g*) enhanced auto fluorescent image, and (*h*) corrected segmentation result based on fluorescence. The pathology section codes on lower row are used to correlate the pathology diagnosis to the images. The segmentation images have three parts: background area, normal tissue (largest areas) and abnormal tissue (smallest areas), respectively.

low achievable specificity. The further image correction process based on autofluorescence images is able to improve the diagnostic effectiveness as shown by the ROC curves in Fig. 10, where a larger AUC (0.792 versus 0.714) and better specificity (80% versus 60%) at cutoff point were shown. We can see that the use of fluorescence imaging does not improve the performance of colposcopy significantly. For over 20 years, researchers have been using the autofluorescence property of cervical tissue for CIN detection and a number of review papers have summarized the feasible excitation–emission pairs as well as discrimination methods between normal and abnormal cervical tissue. However, few progress has been made in technology commercialization and clinical dissemination of this technique for CIN diagnosis. The low diagnostic sensitivity for fluorescence imaging is possibly caused by the fact that autofluorescence property represents a negative disease marker that reveals "cold" spots in fluorescence imaging. In addition, the high individual disparity between patients and the lack of traceable standards for performance evaluation and calibration of the imaging system also contribute to the low sensitivity for fluorescence imaging. Despite its low sensitivity, autofluorescence imaging is still a very useful modality in our application because we do not expect to replace the current diagnostic tools for cervical cancer but to provide a rapid and cost-effective method to guide the clinician's decision in whether and where the cervical tissue will be taken for biopsy and further examination.

4 Conclusions

In this paper, we presented a multimodal colposcopy system for in vivo characterization of CIN. The device was capable of consecutive multispectral reflectance imaging, autofluorescence imaging, and RGB imaging of cervical tissue. Cervical reflectance and autofluorescence spectra were simulated by two optical models based on a two-layered Monte Carlo simulation and an analytical approximation. A second derivative method was applied on the spectrum for multispectral wavelengths optimization. An approved clinical protocol was performed and a classification algorithm was developed for the segmentation of cervical tissue images. In the results, a typical data collection including RGB images, autofluorescence image, and multispectral segmentation image was used to identify cervical tissue as SN and HG type. The results are preliminary but promising. Statistically, the sensitivity and specificity performance of this system related to gold standard of histopathology were 74% and 80%, respectively, with fluorescence images correction. The pilot study demonstrated the potential of this multimodal colposcopy system in cervical cancer detection. The low-cost portable characteristics, the simple operating process, and the simple image segmentation algorithm of the developed multimodal colposcopy leave the system possibility to address the needs for CIN noninvasive characterization in a rapid, cost-effective, and noninvasive fashion in the developing countries. The future work include testing large quantity of patients for statistical analysis, enhancing the accuracy of classification algorithm, and exploring more imaging modalities, such as polarized imaging (sensitive to the distribution of cervical collagen fibers) and laser speckle imaging (sensitive to tissue blood perfusion) in order to improve the sensitivity for the assessment of cervical tissue.

Acknowledgment

The project was partially supported by Natural Science Foundation of China (Nos. 81271527 and 81327803), the Fundamental Research Funds for the Central Universities (WK2090090013), and Chongqing Health and Family planning Committee (2015ZDXM010). The authors appreciate Dr. David Allen of National Institute of Standards and Technology for providing spectral calibration standard and technical support. We appreciate Dr. Zachary Smith of USTC for language editing. The authors are also grateful for the help from Miss. Wenli Zheng, Mr. Jian Ye, and Mr. Qi Gan for device design.

References

[1] Thekkek, N., and Richards-Kortum, R., 2008, "Optical Imaging for Cervical Cancer Detection: Solutions for a Continuing Global Problem," Nat. Rev. Cancer, **8**(9), pp. 725–731.
[2] Parkin, D. M., Bray, F., Ferlay, J., and Pisani, P., 2005 "Global Cancer Statistics, 2002," CA-Cancer J. Clin., **55**(2), pp. 74–108.
[3] Drezek, R. A., Richards-Kortum, R., Brewer, M. A., Feld, M. S., Pitris, C., Ferenczy, A., Faupel, M. L., and Follen, M., 2003, "Optical Imaging of the Cervix," Cancer, **98**(S9), pp. 2015–2027.
[4] Orfanoudaki, I. M., Kappou, D., and Sifakis, S., 2011, "Recent Advances in Optical Imaging for Cervical Cancer Detection," Arch. Gynecol. Obstet., **284**(5), pp. 1197–1208.
[5] Tan, J. H. J., and Wrede, C. D. H., 2011, "New Technologies and Advances in Colposcopic Assessment," Best Pract. Res. Clin.: Obstet. Gynecol., **25**(5), pp. 667–677.
[6] Freeberg, J. A., Serachitopol, D. M., McKinnon, N., Price, R., Atkinson, E. N., Cox, D. D., MacAulay, C., Richards-Kortum, R., Follen, M., and Pikkula, B., 2007, "Fluorescence and Reflectance Device Variability Throughout the Progression of a Phase II Clinical Trial to Detect and Screen for Cervical Neoplasia Using a Fiber Optic Probe," J. Biomed. Opt., **12**(3), p. 034015.
[7] Balas, C., 2001, "A Novel Optical Imaging Method for the Early Detection, Quantitative Grading, and Mapping of Cancerous and Precancerous Lesions of Cervix," IEEE Trans. Biomed. Eng., **48**(1), pp. 96–104.
[8] Mirabal, Y. N., Chang, S. K., Atkinson, E. N., Malpica, A., Follen, M., and Richards-Kortum, R., 2002, "Reflectance Spectroscopy for In Vivo Detection of Cervical Precancer," J. Biomed. Opt., **7**(4), pp. 587–594.
[9] Arifler, D., MacAulay, C., Follen, M., and Richards-Kortum, R., 2006, "Spatially Resolved Reflectance Spectroscopy for Diagnosis of Cervical Precancer: Monte Carlo Modeling and Comparison to Clinical Measurements," J. Biomed. Opt., **11**(6), p. 064027.
[10] Zheng, W., Wang, C., Chang, S., Zhang, S., and Xu, R. X., 2015, "Hyperspectral Wide Gap Second Derivative Analysis for In Vivo Detection of Cervical Intraepithelial Neoplasia," J. Biomed. Opt., **20**(12), p. 121303.
[11] Drezek, R., Sokolov, K., Utzinger, U., Boiko, I., Malpica, A., Follen, M., and Richards-Kortum, R., 2001, "Understanding the Contributions of NADH and Collagen to Cervical Tissue Fluorescence Spectra: Modeling, Measurements, and Implications," J. Biomed. Opt., **6**(4), pp. 385–396.
[12] Drezek, R., Brookner, C., Pavlova, I., Boiko, I., Malpica, A., Lotan, R., Follen, M., and Richards-Kortum, R., 2001, "Autofluorescence Microscopy of Fresh Cervical-Tissue Sections Reveals Alterations in Tissue Biochemistry With Dysplasia," Photochem. Photobiol., **73**(6), pp. 636–641.
[13] Pavlova, I., Sokolov, K., Drezek, R., Malpica, A., Follen, M., and Richards-Kortum, R., 2003, "Microanatomical and Biochemical Origins of Normal and Precancerous Cervical Autofluorescence Using Laser-Scanning Fluorescence Confocal Microscopy," Photochem. Photobiol., **77**(5), pp. 550–555.
[14] Zheng, W., Lau, W., Cheng, C., Soo, K. C., and Olivo, M., 2003, "Optimal Excitation-Emission Wavelengths for Autofluorescence Diagnosis of Bladder Tumors," Int. J. Cancer, **104**(4), pp. 477–481.
[15] Schomacker, K. T., Meese, T. M., Jiang, C., Abele, C. C., Dickson, K., Sum, S. T., and Flewelling, R. F., 2006, "Novel Optical Detection System for In Vivo Identification and Localization of Cervical Intraepithelial Neoplasia," J. Biomed. Opt., **11**(3), p. 34009.
[16] Ren, W., Gan, Q., Wu, Q., Zhang, S., and Xu, R., 2015, "Quasi-Simultaneous Multimodal Imaging of Cutaneous Tissue Oxygenation and Perfusion," J. Biomed. Opt., **20**(12), p. 121307.
[17] Zhang, S., Gnyawali, S., Huang, J., Ren, W., Gordillo, G., Sen, C. K., and Xu, R., 2015, "Multimodal Imaging of Cutaneous Wound Tissue," J. Biomed. Opt., **20**(1), p. 016016.
[18] Milbourne, A., Park, S. Y., Benedet, J. L., Miller, D., Ehlen, T., Rhodes, H., Malpica, A., Matisic, J., Van Niekirk, D., Atkinson, E. N., Hadad, N., Mackinnon, N., Macaulay, C., Richards-Kortum, R., and Follen, M., 2005, "Results of a Pilot Study of Multispectral Digital Colposcopy for the In Vivo Detection of Cervical Intraepithelial Neoplasia," Gynecol. Oncol., **99**(3), pp. S67–S75.
[19] Gustafsson, U. P., McLaughlin, E., Jacobsen, E., Hakansson, J., Troy, P., DeWeert, M. J., Svanberg, K., Palsson, S., Thompson, M. S., and Svanberg, S., 2003, "In-Vivo Fluorescence and Reflectance Imaging of Human Cervical Tissue," Proc. SPIE, **5031**, pp. 521–530.
[20] Redden Weber, C., Schwarz, R. A., Atkinson, E. N., Cox, D. D., Macaulay, C., Follen, M., and Richards-Kortum, R., 2008, "Model-Based Analysis of Reflectance and Fluorescence Spectra for In Vivo Detection of Cervical Dysplasia and Cancer," J. Biomed. Opt., **13**(6), p. 064016.
[21] Wang, L., Jacques, S. L., and Zheng, L., 1995, "MCML—Monte Carlo Modeling of Light Transport in Multi-Layered Tissues," Comput. Methods Programs Biomed., **47**(2), pp. 131–146.
[22] Prahl, S. A., 2002, "Simple and Accurate Approximations for Reflectance From a Semi-Infinite Turbid Medium," OSA Biomedical Topical Meeting, Miami Beach, FL, Apr. 7, Paper No. TuF4, pp. 613–614.
[23] Myers, D. E., Anderson, L. D., Seifert, R. P., Ortner, J. P., Cooper, C. E., Beilman, G. J., and Mowlem, J. D., 2005, "Noninvasive Method for Measuring Local Hemoglobin Oxygen Saturation in Tissue Using Wide Gap Second Derivative Near-Infrared Spectroscopy," J. Biomed. Opt., **10**(3), p. 034017.
[24] Chang, S. K., Arifler, D., Drezek, R., Follen, M., and Richards-Kortum, R., 2004, "Analytical Model to Describe Fluorescence Spectra of Normal and

Preneoplastic Epithelial Tissue: Comparison With Monte Carlo Simulations and Clinical Measurements," J. Biomed. Opt., **9**(3), pp. 511–522.
[25] Parker, M. F., Mooradian, G. C., Okimoto, G. S., O'Connor, D. M., Miyazawa, K., and Saggese, S. J., 2002, "Initial Neural Net Construction for the Detection of Cervical Intraepithelial Neoplasia by Fluorescence Imaging," Am. J. Obstet. Gyencol., **187**(2), pp. 398–402.
[26] Park, S. Y., Follen, M., Milbourne, A., Rhodes, H., Malpica, A., MacKinnon, N., MacAulay, C., Markey, M. K., and Richards-Kortum, R., 2008, "Automated Image Analysis of Digital Colposcopy for the Detection of Cervical Neoplasia," J. Biomed. Opt., **13**(1), p. 014029.
[27] Pogue, B. W., Mycek, M.-A., and Harper, D., 2000, "Image Analysis for Discrimination of Cervical Neoplasia," J. Biomed. Opt., **5**(1), pp. 72–82.
[28] Orfanoudaki, I. M., Themelis, G. C., Sifakis, S. K., Fragouli, D. H., Panayiotides, J. G., Vazgiouraki, E. M., and Koumantakis, E. E., 2005, "A Clinical Study of Optical Biopsy of the Uterine Cervix Using a Multispectral Imaging System," Gynecol. Oncol., **96**(1), pp. 119–131.
[29] Pogue, B. W., Kaufman, H. B., Zelenchuk, A., Harper, W., Burke, G. C., Burke, E. E., and Harper, D. M., 2001, "Analysis of Acetic Acid-Induced Whitening of High-Grade Squamous Intraepithelial Lesions," J. Biomed. Opt., **6**(4), pp. 397–403.